8
Correction for Partial Volume Effects in Emission Tomography

O.G. Rousset* and H. Zaidi†

1. Introduction

Despite 25 years of continual improvement of the physical characteristics of positron emission tomography (PET) and single-photon emission computed tomography (SPECT) instruments, including crystal technology, improved electronics, and faster computers, PET and SPECT are still plagued with relatively low spatial resolution compared to anatomy-oriented imaging devices such as magnetic resonance (MR) imaging or x-ray computed tomography (CT). Further, in order to accurately explore cell metabolism, reproducibility and sensitivity of the data analysis procedures must at least match the subtle changes occurring in metabolism that one tries to investigate. While it is of primary importance to compensate for physical effects such as interaction of photons with matter resulting in their attenuation (see Chapter 6) and scattering (see Chapter 7), geometry-dependent interactions between the imaging system and the distribution of radioactivity in the field-of-view must also be accounted for. This includes correction methods used to account for collimator response in SPECT (see Chapter 5). Despite all the efforts aimed at improving the quality and meaningfulness of emission tomography (ET), there remains the need to correct for limited resolution (or *partial volume*) effects if one wants to obtain absolute image quantification.[1,2]

Partial volume effects (PVE's) have been shown to result in large bias in the estimate of regional radioactivity concentration, both in experimental phantom and simulation studies. Partial volume is usually addressed in the context of "small" regions, i.e., with dimensions smaller than around 2-4 times the full-width at half-maximum (FWHM) of the scanner's point-spread function (*PSF*). It is rather hard indeed to find for example a single

*Dr O.G. Rousset, Department of Radiology, Johns Hopkins Medical Institutions, Baltimore, MD 21287 USA
†PD Dr H. Zaidi, Division of Nuclear Medicine, Geneva University Hospital, CH-1211 Geneva, Switzerland

brain structure that can elude partial volume given the spatial resolution of current emission tomography systems.[3]

In the presence of tissue atrophy, such as in the case of Dementia of Alzheimer Type (DAT), the signal is diluted even further since the scanner's resolution cell contains even less cortical grey matter. What is important to the clinician and research investigator is the ability to distinguish the loss of radioactivity due to increase in partial volume effects from the true loss of tissue function. In the case of dynamic studies of the heart and brain, time-varying contrasts between the target region and its surrounding lead to distortion of true tissue time-activity curves and subsequent underestimation of physiological parameters.

The purpose of this chapter is to introduce basic notions and describe correction methods for partial volume effects in emission tomography as well as their evaluation strategies.

2. The Problem of Partial Volume Effect

The general problem of partial volume effect was first introduced in the context of the early generation of X-ray CT and PET scanners.[4] With crystal size soaring at over 2 cm thick, substantial part of the anatomical region under study would only partially occupy the imaging volume resolution cell. In emission tomography, this phenomenon of *partial volume* came to include both the loss of detection sensitivity in the axial direction (slice thickness), as well as in-plane resolution effect resulting from in-plane detector response and filtering of the projection prior to backprojection.

The limited spatial resolution of emission tomography depends on a number of factors from various sources: i) physical, such as positron range and non-colinearity of emitted annihilation photons (in PET), scattered radiation (in SPECT and PET), ii) instrumental, such as scintillation crystal size, their detection efficiency and geometrical arrangement, or collimator geometry (in SPECT) and iii) methodological, such as the choice of parameters for image acquisition and reconstruction processes. Finally, even if this will not influence the resolution of the system *per se*, the choice of the regions-of-interest (RoI) for extracting regional activity concentrations will further modulate the degree of recovery of actual tracer distribution.

Due to the imperfections of the imaging system, the response of the scanner to a point source of activity, or *point-spread function* (*PSF*) , will show a bell shape. The full width of the *PSF* taken at half the maximum of the profile (or full-width at half-maximum—FWHM) is generally taken as the measure of spatial resolution (Figure 1).

If we consider the simple one-dimensional case where an object possesses one of its dimensions smaller that 2-3 times the spatial resolution along that particular direction, a profile through the produced image will show an underestimation of true tracer concentration (Figure 2). The signal profile of this

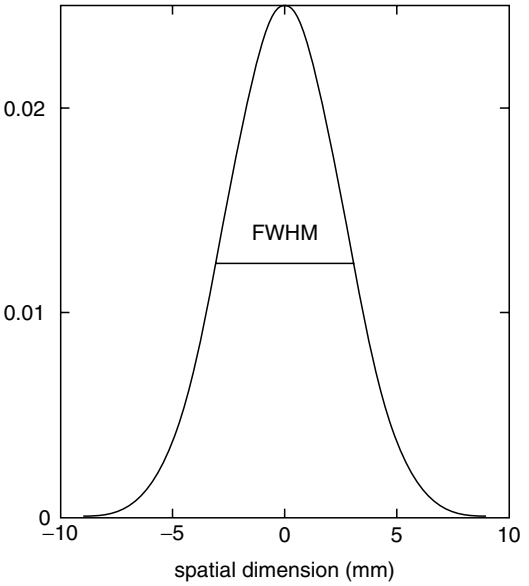

FIGURE 1. Mono-dimensional Gaussian function representing typical spatial response function, or point-spread function (*PSF*), of modern emission tomographs. Spatial resolution is usually given in terms of full-width-at-half-maximum (FWHM) of the *PSF*, which has been chosen equal to 6 mm in this illustration.

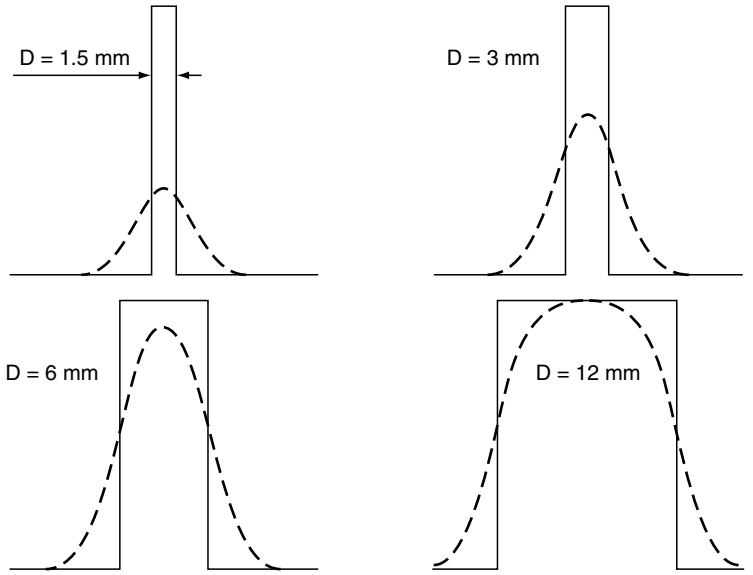

FIGURE 2. Schematic illustration of the partial volume effect. The observed signal (dashed line) is underestimated compared to true profiles (solid lines) depending on object size D with respect to the scanner's spatial resolution (chosen as equal to 6 mm (FWHM) in this example). We see clearly that in order for the object D to exhibit 100% of true original activity, its dimension needs to be greater than $2\times$FWHM ($D > 12$ mm).

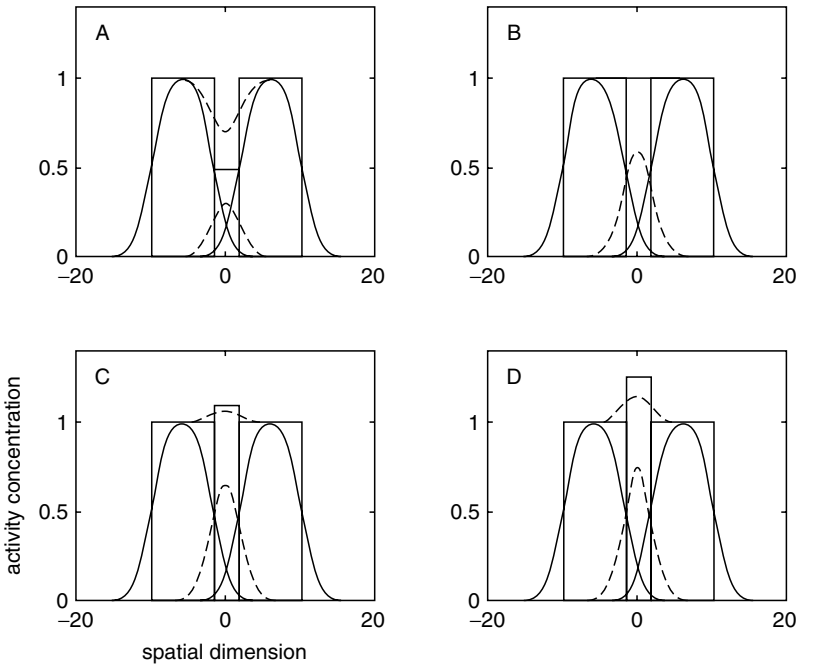

FIGURE 3. More general definition of partial volume effect(s). When a small object of width D (D=6 mm in this illustration) is surrounded by background activity, the observed signal will result from the addition of the target object signal (dashed line) plus a contamination component referred to as "spill-over" or "spill-in". When the activity in the target object is smaller than in the surrounding, we observe an overestimation of its activity (A). In the absence of image contrast, i.e., if the target activity is the same as in the surrounding (B), the observed signal will be equal to the true signal as activity spilled-out is exactly compensated by activity spill-in. When the activity in the target object is above that of the background, the observed signal is underestimated (C and D).

isolated object is further distorted by the presence of neighbouring activity (Figure 3). The goal of partial volume correction (PVC) is to be able to account for both the loss of signal due to the limited size of the object with respect to resolution, and the signal contamination coming from the rest of the image.

3. Theoretical Considerations: Object-Image Relationship

For a non-linear system, with a spatially variant point-spread function $h(r)$, the resulting image $g(r)$ of a distribution of activity $f(r)$ can be written as:

$$g(r) = \int_{\Re} h(r, r', f(r'))\, dr' \tag{1}$$

where r and r' are the vectors in image and object space respectively. For a linear system we have:

$$g(r) = \int_{\Re} h(r, r')\, f(r') dr' \tag{2}$$

where $h(r, r')$ represents the system's *PSF*. Those two last equations represent the most general description of the image formation process, where the *PSF* is a function of the spatial coordinates in both spaces (object and image), and is referred to as spatially variant. In the case where the response to a point source of activity is the same for all the points in the object space, the *PSF* is said to be spatially invariant. In this case, h only depends on the difference in coordinates r-r' since the response to a point source depends only on the relative distance between these 2 points in the image plane. For a spatially invariant, non-linear system, Eq. (2) becomes:

$$g(r) = \int_{\Re} h(r - r', f(r')) dr' \tag{3}$$

Whereas for a spatially invariant, linear system:

$$g(r) = \int_{\Re} h(r - r') f(r')\, dr' \tag{4}$$

We recognize here the convolution integral: the image is equal to the convolution of the object distribution with the *PSF* of the imaging system. The *PSF* transfers the information from the object space to the image space and incorporate all the geometrical infidelities of the imaging system. It is therefore not surprising that the attempt to compensate for those degradations be referred to as a "deconvolution" process. It is worth emphasizing here that this term should in theory only be applicable in situation where the *PSF* is a spatially-invariant function.

4. The General Problem of Image Restoration

If we concentrate on the case where the imaging system is linear and spatially invariant, we have seen (Eq. 4) that the object $f(r)$ and the image $g(r)$ are linked by the convolution integral that can be simply written as:

$$g(r) = h(r) \otimes f(r) \tag{5}$$

where $\otimes$ represents the convolution operator. In Fourier space, the convolution becomes a simple multiplication of the Fourier transforms $H(u)$ and $F(u)$ of the functions $h(r)$ and $f(r)$, respectively, (convolution theorem).We can then write:

$$G(u) = H(u) \times F(u) \tag{6}$$

where u represents the spatial frequency corresponding to the spatial coordinate r. The relationship between a function and its Fourier transform being given by:

$$F(u) = \int_{\Re} f(r) \times e^{-2\pi i u r} dr \tag{7}$$

and

$$f(r) = \int_{\Re} F(u) \times e^{2\pi i u r} du \tag{8}$$

Equation (8) indicates that the object f can be separated into its spatial frequency components u and how these elements can be recombined to recover the original object f. This representation in Fourier space contains the same information than in real space, only in a different form. It is then clear that the Fourier transform H of the *PSF* h corresponds to the fraction of the object distribution component of spatial frequency u that is transferred to the image distribution at the same spatial frequency. H regulates the transfer of information for each spatial frequency, and is often termed the *modulation transfer function* (*MTF*) . If the imaging system was perfect (i.e., $H = 1$), the image would be a perfect representation of the object, and h would be a Dirac function (*PSF* infinitely narrow). Unfortunately, for every imaging system, and in particular for PET and SPECT, we observe a dispersion of the system *PSF* which corresponds to a decrease of the *MTF* magnitude with increasing spatial frequency. It is therefore clear that there is a loss of spatial information for the high spatial frequencies. If one thinks of recovering this information by performing a direct deconvolution, it becomes clear that we need to invert Eq. (6):

$$F(u) = G(u)/H(u) \tag{9}$$

thus

$$f(r) = \int_{\Re} \frac{G(u)}{H(u)} e^{2\pi i u} du \tag{10}$$

The practical use of this simple procedure is not very reasonable if we consider that H decreases in magnitude with increasing spatial frequency. It is at those high frequencies that the image becomes dominated by noise, that the deconvolution suggested in Eq. (10) would amplify to unacceptable levels.

In fact, the image formation process given in Eq. (2) could present the false impression that object and image spaces are only connected by geometrical transformations. In practice, the images are contaminated by a whole variety of noise of various origins. A more accurate description of the image formation process is hence the following for a linear system:

$$g(r) = \int_{\Re} h(r, r')\, f(r')dr' + \eta(r) \tag{11}$$

where η represents the noise distribution in the image (assumed to be additive here). There is no unique solution to this equation, and the problem is said to be "ill-posed", meaning that a small perturbation in the image can lead to large errors in the solution. Image restoration consists in finding the best solution to Eq. (11) while limiting noise amplification resulting from the correction process. If we consider that the image can be written as the effect of an operator on the object, plus a noise component, we can then write Eq. (11) in the form:

$$g = Hf + \eta \tag{12}$$

If we apply the inverse operator, we obtain:

$$H^{-1}g = H^{-1}Hf + H^{-1}\eta \tag{13}$$

If we define a measurement of the object as being the inverse of H applied to g, then:

$$\hat{f} = f + H^{-1}\eta \tag{14}$$

This equation indicates that the "processed" image $\hat{f}$ is equal to the real object plus a term representing the noise amplification. If the operator H is singular, this image can not even be obtained, and even if H is only slightly ill-conditioned, the second term of Eq. (14) becomes predominant and will invalidate the correction method.

5. Theoretical Activity Recovery of Known Size Objects

Typical *PSF* of emission tomography systems can be approximated by a Gaussian function of a few millimetres FWHM. The partial volume effect on spherical objects of inner radii varying from 4 to 15.5 mm, for emission tomography systems with spatial resolution varying between 2 and 10 mm FWHM, are illustrated in Figure 4. It is worth noticing that the smallest sphere (4 mm) is hardly visible when using a system with similar spatial resolution and not detectable at all for systems with lower spatial resolution (> 4 mm).

By definition, a normalized Gaussian aperture function of the spatial function *r(x,y,z)* can be expressed as:

$$h(r) = \frac{(2\pi)^{-3/2}}{\sigma_{S_x}\sigma_{S_y}\sigma_{S_z}} \times \exp\left(-\frac{1}{2}\left[\frac{x^2}{\sigma_{S_x}^2} + \frac{y^2}{\sigma_{S_y}^2} + \frac{z^2}{\sigma_{Sz}^2}\right]\right) \tag{15}$$

where σ_{Sx}, σ_{Sy}, and σ_{Sz} represent the standard deviation in the x, y, and z directions. This symmetric function has a maximum value of $1/\sqrt{2\pi\sigma_{S_x}}$ in 1-D, $1/\sqrt{2\pi\sigma_{S_x}\sigma_{Sy}}$ in 2-D, and $1/\sqrt{2\pi\sigma_{S_x}\sigma_{Sy}\sigma_{Sz}}$ in 3-D.

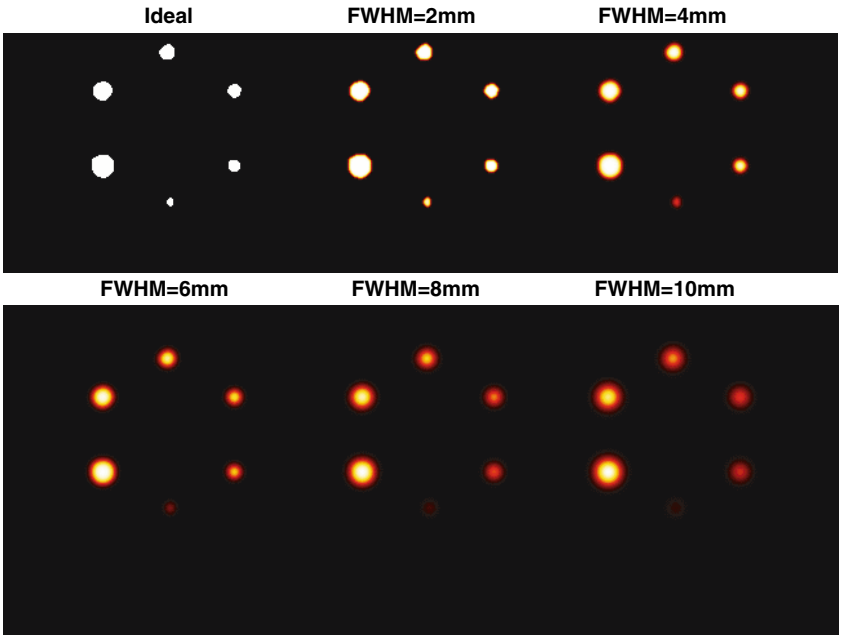

FIGURE 4. Illustration of the partial volume effect using simulated spheres of 4.0, 7.5, 8.5, 11.0, 13.0, and 15.5 mm inner radii for imaging systems with spatial resolution FWHM varying between 2 and 10 mm.

If we consider the Gaussian function definition given in Eq. (15) and the definition of the spatial resolution in terms of the FWHM of the scanner's *PSF*, we can relate the FWHM to the standard deviation σ as follows:

$$\exp\left(-\frac{1}{2}\left(\frac{FWHM}{2\sigma}\right)^2\right) = 1/2 \Leftrightarrow \frac{FWHM}{2\sigma} = \sqrt{2\ln 2} \approx 1.18 \qquad (16)$$

If the Gaussian aperture function presented in Eq. (15) is convolved with a Gaussian object of standard deviations σ_{Ox}, σ_{Oy}, and σ_{Oz} along x, y, and z, the result can be directly assessed after Fourier transform and multiplication in the frequency domain, and can be expressed as:

$$g(r) = \frac{\sigma_{O_x}\sigma_{O_y}\sigma_{O_z}}{\sqrt{\left(\sigma_{O_x}^2+\sigma_{Sx}^2\right)\left(\sigma_{O_y}^2+\sigma_{Sy}^2\right)\left(\sigma_{O_z}^2+\sigma_{Sz}^2\right)}} \times \exp\left(-\frac{1}{2}\left[\frac{x^2}{\sigma_{O_x}^2+\sigma_{Sx}^2}+\frac{y^2}{\sigma_{O_y}^2+\sigma_{Sy}^2}+\frac{z^2}{\sigma_{O_z}^2+\sigma_{Sz}^2}\right]\right) \qquad (17)$$

The results for 1-D and 2-D objects can be readily derived from the previous equation by dropping the z and y variables respectively. For

instance, the maximum recovery coefficient (RC) for a 2-D Gaussian object of identical standard deviation along x and y (i.e., $\sigma_{Ox} = \sigma_{Oy} = \sigma_O$), becomes:

$$RC = \frac{(\sigma_O/\sigma_S)^2}{1 + (\sigma_O/\sigma_S)^2} \tag{18}$$

We can predict analytically the maximum RC values in the case of objects of simple geometrical shape. In the case of a bar of width D that is the only dimension to suffer from partial volume effects, the recovery coefficient can be expressed by the convolution integral:

$$\begin{aligned} RC(x/\sigma) &= \int_{-D/2}^{D/2} \frac{1}{\sqrt{2\pi}\sigma} \exp\left(-\frac{1}{2}\frac{x^2}{\sigma^2}\right) dx \\ &= erf\left(\frac{D/2}{\sqrt{2}\sigma}\right) \end{aligned} \tag{19}$$

where

$$erf\left(\frac{u}{\sqrt{2}\sigma}\right) = \int_{-\infty}^{u} \frac{1}{\sqrt{2\pi}\sigma} \exp\left(-\frac{\omega^2}{2\sigma^2}\right) d\omega \tag{20}$$

and represents the error function.[5] The calculation is also possible in 2-D in the case of a cylinder of elliptical section whose length is large with respect to the resolution along the z dimension.[6] For an elliptical section given by:

$$x^2/b^2 + y^2/c^2 = R^2 \tag{21}$$

then

$$\begin{aligned} &RC(R/\sigma) = 1 - \exp(-R^2/2\sigma^2) \\ &RC(D/FWHM) = 1 - \exp(-\ln 2 \times D^2/FWHM^2) \quad \because D = 2R \end{aligned} \tag{22}$$

In the case where a sphere of radius R is centred on an isotropic Gaussian function of standard deviation σ, the maximum value for the 3-D recovery coefficient that one can obtain in the image is given by:

$$RC_{3D} = \frac{1}{(2\pi)^{3/2}\sigma^3} \int_{-R}^{R} dz \int_{-R}^{R} dy \int_{-R}^{R} dx \left(\exp\left(-\frac{x^2 + y^2 + z^2}{2\sigma^2}\right)\right) \tag{23}$$

The result of this integral is proposed in the work published by Kessler *et al.*[7] and is illustrated in figure 5 along with the results obtained in 1-D and 2-D. This calculation was expended to the more general case where the sphere's centre is shifted by an amount Z_p with respect to the centre of the Gaussian aperture function:

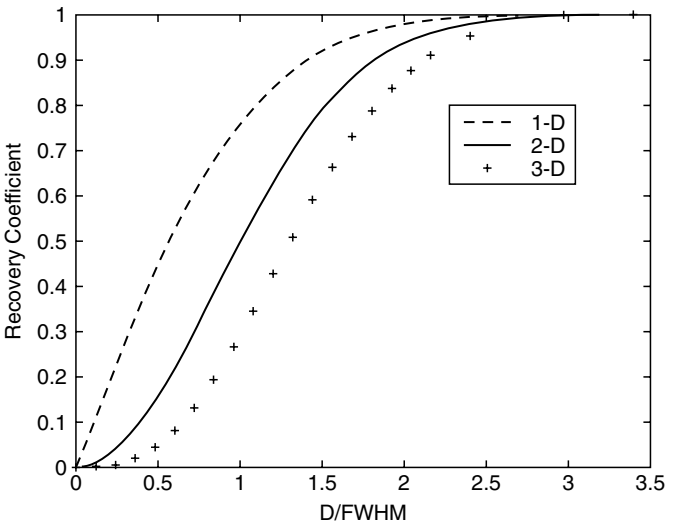

FIGURE 5. Maximum theoretical recovery coefficients (RC) resulting from the computation of the convolution integrals for various geometries: bar (1-D), cylinder (2-D), and sphere (3-D), plotted as a function of their spatial characteristic D normalized to the image resolution in terms of its FWHM.

$$RC(R/\sigma, Z_p/\sigma) = erf\left(\frac{R - Z_p}{\sqrt{2}\sigma}\right) - erf\left(\frac{-R - Z_p}{\sqrt{2}\sigma}\right) - \frac{1}{\sqrt{2\pi}}\frac{\sigma}{Z_p} \exp\left(-\frac{R^2 + Z_p^2}{2\sigma^2}\right) \times \left[\exp\left(\frac{R \times Z_p}{\sigma^2}\right) - \exp\left(-\frac{R \times Z_p}{\sigma^2}\right)\right] \tag{24}$$

For every combination of object and impulse function (*PSF*) , a whole range of *RC* values are possible, with *RC* reaching a maximum when the object and the *PSF* have maximum overlap.[8]

It should be noted here that the *RC* defined by Hoffman *et al.*[9] characterizes only one of the two aspects of the partial volume effect. It represents in fact the fraction of TRUE activity contained in the measurement in the absence of activity other than that present in the object (''cold'' background). This concept does not take into account the presence of a ''warm'' surrounding medium that contaminates the measurements of the ''hot'' spots. We can nevertheless mention the introduction of the concept of contrast recovery coefficient (*CRC*)[7] that reflects the rate of recovery that lies above the surrounding medium (BKG), i.e., *CRC=(obs-BKG)/(TRUE-BKG)*. This parameter is only justified in the case where the BKG is not itself subject to PVE's, and is of known and uniform activity concentration.

6. Partial Volume Correction Strategies

Attempts to compensate for partial volume effects date back to the time where they were first pointed out as a serious limitation in quantitative analysis. The reference paper is probably that of Hoffman *et al.*[9] where he proposed the computation of recovery coefficients from the known geometry of the objects being imaged and their position relative to the centre of a given PET slice. From the same group, Mazziotta then predicted the recovery coefficients for numerous brain structures based on their approximation by a series of non-overlapping spheres.[10] Although the partial volume phenomenon was first addressed in the context of "hot" objects in a "cold" background, emphasizing on the apparent loss of radioactivity due to the small object size with respect to the spatial resolution of the system,[9] it became obvious that it was necessary not only to account for activity "spilling-out" of the "hot" region, but that "spill-in" from the surrounding usually "warm" area should also be accounted for in the regional measurements.[7] Several authors attempted some sort of partial volume correction by applying the recovery coefficients described by Hoffman as well as those derived from Kessler's formulation.[11,12]

Some correction methods require only the original emission data. These include methods making all the necessary corrections for physical effects at the projection level, such as in the method proposed originally by Huesman *et al.*[13] for scatter correction. Iterative reconstruction techniques that incorporate a blurring model in their iterative scheme have been proposed to compensate for the inherent blurring of SPECT.[14,15] This aspect is covered in detail in Chapter 5. There has also been a great deal of search for image processing tools that would restore, or at least visually enhance, the noisy images obtained in emission tomography. Those can be regrouped into the general class of filters used during image reconstruction (low-pass filtering), and those used post-reconstruction for the purpose of restoration filtering. The latter include methods such as Wiener's filtering widely used in evoked potential, and investigated as a way of suppressing noise while maintaining the signal content of time-activity curves.[16,17] In SPECT, depth-dependent blurring can be corrected by first back-projecting each projection and then applying a depth-dependent Wiener filter row by row.[18] Finally, another approach that does not require additional data is based on the computation of correction factors during mathematical modelling of kinetic data, such as regional cerebral blood flow (CBF) measurement with PET, both in the heart[19] and brain.[20]

A distinct class of correction methods require the definition of the various objects being imaged in addition to the characterization of the scanner's *PSF*. These include anatomy-based post-reconstruction correction methods that make use of concomitant high-resolution structural information from

MR imaging or CT.[21-27] Being the most popular methods, those will be described in details later in this section.

Finally, empirical methods based on the derivation of correction factors from experiments with physical test objects remain an active way of characterizing partial volume effects.[28,29]

6.1 *Correction Methods based on Physical Phantom Experiments*

Such empirical methods mimic the object (radioactivity distribution) by a series of simple geometrical shapes (cylinders, spheres) to derive correction factors for actual anatomical structure that can be approximated by a simple shape or a linear combination of simple geometrical shapes. Some researchers have proposed to describe the effect of scatter counts and partial volume on the *PSF* by a series of functions with parameters derived from physical phantoms experiments.[28] This method requires the availability of a realistic physical phantom of the organ or tissue of interest, although empirical rules allow to deriving the *PSF* of an arbitrary object from the *PSF* of a known object.

Also, the estimation of the arterial input function required for the absolute quantification of fast dynamic studies of tracer pharmacokinetics, has been proposed based on its estimation from a large artery after correction for PVE's. Such correction factors can be derived from imaging cylindrical distribution of activity of various diameters and for various levels of background activity.[29] This method is based on Kessler's formulation of the hot spot recovery coefficient (*HSRC*) or ratio of image activity concentration to the true activity concentration in a "hot" isolated region, and cold spot recovery coefficient (*CSRC*) or ratio of image activity in "cold" spot to true background concentration.[7,30] In this case, in the presence of the 2-component system (target+background), according to the formulation of Kessler, the observed estimate of activity within the target region (e.g., arterial vessel) can be expressed as:

$$t_{target} = HSRC \times T_{target} + CSRC \times T_{background} \tag{25}$$

with $T_{background}$ representing the true radioactivity concentration of the background region, and t_{target} is the target radioactivity concentration observed with the imaging system. Under the condition that the target region is totally surrounded by the background region, we have the relationship:

$$HSRC + CSRC = 1 \tag{26}$$

By substituting *CSRC* from Eq. 26 in Eq. 25, we can estimate the corrected activity within the target region:

$$T_{target} = \frac{1}{HSRC}(t_{target} - T_{background}) + T_{background} \tag{27}$$

We can note that the *HSRC* is generally simply referred to as the recovery coefficient. In the present case, the application of this approach assumes that the background activity can be accurately assessed directly from the emission image. In other words, the background is assumed not to be affected by partial volume. This method also assumes that the size of e.g., the vessel, can be accurately estimated. This is a crude approach in its assumption on large surrounding homogeneous background, but has the advantage of only requiring the estimation of the *RC* of the target region. Similarly, recovery coefficients derived from phantom studies have been proposed to correct for partial volume effects in SPECT myocardial perfusion studies.[31] A similar approach was adopted to demonstrate the feasibility of such correction in a clinical setting where the anatomical structures can be approximated by simple geometrical objects.[30] The study concluded that a recovery correction is feasible only for PET data down to lesions of size ~1.5 × FWHM.

However, this kind of approach represents a real technical challenge for more complex organs where anatomical variability or the presence of anatomical abnormalities cannot be addressed by a single physical model. While physical models of the heart in various sizes are available (Data Spectrum, Hillsborough, NC), there is no existing brain phantom that can reproduce the brain circumvolutions or structures smaller than about 10 ml in volume. However, even in the absence of gross abnormalities such as tissue atrophy, normal anatomical variability especially that found in the human brain would not favour the use of a single physical model for correction purposes. However, some authors have for instance proposed a method to overcome the problem of axial under-sampling of emission tomographs based on phantom experiments.[32] Their method make use of a human basal ganglia phantom to validate their assumption according to which the intensity profile in the axial direction can be accurately assessed by Gaussian fitting in order to derive correction factors that compensate for the non-uniform axial response function of the scanner, making the signal independent from axial positioning of the head.

6.2 Reconstruction-based Correction Methods

Such methods may or may not require the availability of supplementary structural information from e.g., MR imaging. Because of the inherent degradation of spatial resolution during filtered backprojection, there is a great deal of research for statistical reconstruction approaches that would overcome this problem of resolution loss while dealing with the intrinsic Poissonian nature of the noise. For example, iterative reconstruction methods such as those derived from the Maximum-Likelihood Expectation-Maximization scheme[33] can incorporate all kind of information such as scatter or spatial variation of the system's *PSF* to compensate for non-stationary resolution (see Chapter 4). Those methods have been explored both in SPECT[14,34-36] and PET.[37]

Some other iterative reconstruction methods not only incorporate some model of the scanner's *PSF*, but can also incorporate *a priori* anatomical information from e.g., MRI, in an attempt to compensate for partial volume effect, both in SPECT[38] and PET.[39,40] However those methods still fail to account for resolution effects in the axial direction, which remains the predominant source of partial volume effects.

Another class of correction schemes, based on quantification directly in projection space, is derived from the early work of Huesman *et al.*[13] and was extended to include not only scatter but also spatial resolution effects, both in the heart[41] and tumour imaging.[42] The major advantage of this approach is its ability to derive accurate figure of regional variance. However this kind of methods cannot account for partial volume effects of objects with cross-section about the size of the intrinsic resolution of the scanner, and has yet to be extended in 3-D.

6.3 Post-reconstruction Correction Methods

It becomes increasingly common, if not systematic, to have access to both the functional information from emission tomography, together with its underlying anatomy defined from high-resolution, structure-oriented, scanning devices such as MR or CT. The combined use of anatomical and functional data allows for a more accurate identification and definition of regions used for the assessment of regional tracer concentration. This trend is also reflected in the development of PET/CT and PET/MRI devices that allow access to both types of information simultaneously, thus avoiding the problem of inter-modality spatial realignment errors (see Chapter 9).

Such correction method consists in solving the imaging equation (Eq. 2). Due to the stochastic and Poissonian form of the signal, it is not possible to simply deconvolve the image with the inverse of the *PSF* without unbearable noise magnification (see Chapter 4).

In order to reduce the number of unknowns in the imaging equation, i.e., minimizing the noise propagation issue, it is necessary to perform a data reduction, i.e., a segmentation of the anatomical information provided by CT or MR imaging. It is therefore assumed that each "segment" of the "activity distribution model" represents a distinct and homogeneous activity distribution. If we consider that the activity distribution $f(r)$ consists of N tissue components of true activity T_i, the resulting image $g(r)$ for a linear system (spatially invariant or not) can be written as the imaging equation:

$$\begin{aligned} g(r) &= \sum_{i=1}^{N} \int_{D_i} h(r, r')\, f_i(r)\, dr + \eta(r) \\ \text{with } & \bigcup_{i=1}^{N} f_i(r) = f(r) \end{aligned} \tag{28}$$

There is no assumption here on the noise characteristics of the image. Although Poissonian in essence, the final noise $\eta(r)$ in the image includes also components from attenuation, scatter, or other type of corrections during data acquisition and reconstruction. Since the partial volume solutions proposed here do not call for the explicit characterization of a noise model, we will omit the noise component in the subsequent equations.

6.3.1 Pixel-guided Approach

If one seeks to recover the entire true activity distribution $f_i(r)$ within tissue component D_i, there are N unknowns, the true image distribution of activity of each tissue component of the tracer distribution model, but only one equation, the emission image $g(r)$. Several authors proposed to solve this equation, first with $N=1$ to compensate for signal dilution in spaces void of activity.[43] Compensating for dilution of radioactivity in non-active tissues such as cerebro-spinal fluid is more important in the case of tissue atrophy, as the decrease of metabolism seen with increased tissue atrophy might be confounded by the loss of signal consequent to increased partial volume effect. For example, the decline in blood flow observed with PET has been shown not to decline with age after correcting for tissue atrophy using this method.[44] These techniques make use of an anatomical mask defined from MRI or CT, and by assigning pixels corresponding to the cerebral tissue (i.e., grey and white matter) a value of 1, and the space occupied by non-cerebral tissue being kept at 0. This is equivalent to defining an anatomical mask $f_1(r)$ as follows:

$$f_1(r) = \begin{cases} 1 & r = cerebral\ tissue \\ 0 & r = non - cerebral \end{cases} \tag{29}$$

As discussed earlier (Eq. 5), if we consider the point-spread function h of the imaging system as being a spatially invariant function, the equation becomes a simple convolution. The next step of this correction method hence consists in convolving the binarized volume $f_1(r)$ at the scanner's resolution. The PET image in divided by this "low resolution" mask in order to obtain images corrected for dilution of radioactivity in non-active spaces. Hence, the very approximate of the true activity distribution is given by:

$$f(r) = \frac{f_1(r)g(r)}{f_1(r) \otimes h(r)} \tag{30}$$

This equation being derived from the approximation:

$$\frac{f(r)}{f(r) \otimes h(r)} \approx \frac{f_1(r)}{f_1(r) \otimes h(r)} \tag{31}$$

It can be seen that the approximation proposed in Eq. (31) is only justified when $f(r)$ possesses the same spatial characteristics as those defined by the anatomical mask $f_i(r)$. This approach ignores the difference in tracer uptake between grey and white matter.

An extension to a more heterogeneous distribution of the tracer was later proposed, this time with a more realistic mask that makes the distinction between grey and white matter to account for white matter activity contribution to measurements of grey matter activity concentration.[22] We have this time the problem that the number of unknowns is now equal to $N = 2$, while the number of equations has not changed (only one). The way these authors overcame this problem is by transforming one of the unknowns into a known variable. They assume that the true white matter activity can be accurately measured from a large remote white matter area in the emission image (Figure 6). This new mask can be defined as follows:

$$f(r) = \begin{cases} f_1(r) & r = \textit{Grey matter} \\ f_2(r) & r = \textit{White matter} \\ f_3(r) & r = \textit{background \& CSF} \end{cases} \tag{32}$$

Where e.g., $f_1(r) = 1$ for pixels identified as Grey matter, and $f_1(r) = 0$ elsewhere. The tissue components Grey, White, and $BKG + CSF$ are obtained by segmentation of the MR images realigned with the PET image volume. Figure 6 illustrates the general principle of MR-guided PVC in functional brain imaging.

By considering that the radioactivity concentrations in white matter and CSF spaces are constant, and that those components do not suffer themselves from partial volume thanks to their important dimensions with respect to the imaging system resolution, the PET image can be written as:

$$\begin{aligned} g(r) &= f(r) \otimes h(r) \\ &= [T_1 f_1(r) + T_2 f_2(r) + T_3 f_3(r)] \otimes h(r) \\ &= T_1 f_1(r) \otimes h(r) + [T_2 f_2(r) + T_3 f_3(r)] \otimes h(r) \end{aligned} \tag{33}$$

where T_2 and T_3 are *known* constants representing the true activity of the white matter and background plus CSF, respectively. After rearranging the previous equation, one can write:

$$T_1(r) = \frac{g(r) - T_2 f_2(r) \otimes h(r) - T_3 f_3 \otimes h(r)}{f_1(r) \otimes h(r)} \tag{34}$$

White matter activity T_2 is considered as being uniform throughout the brain whose activity concentration is considered as being accurately estimated from a measurement in the pons, assumed to elude partial volume due to its large cross-sectional size. This value is assigned to the low-resolution white matter image $f_2(r) \otimes h(r)$, and then subtracted from the PET image $g(r)$. These authors proposed to do the same with background + CSF compartment, although one might wonder whether the measured value for that compartment is not the result of spillover from adjacent tissue plus noise. However, for increased realism, and to make a distinction in grey matter tracer uptake, these authors extended this elimination-substitution

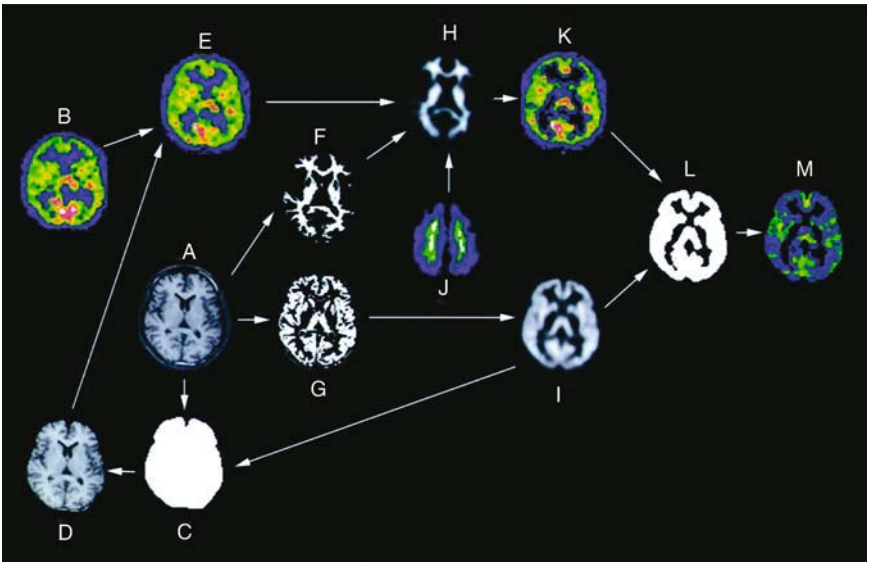

FIGURE 6. Schematic representation of the different steps required for MRI-guided correction for partial volume effect illustrating the original MR (A) and SPECT (B) images, binary mask for whole brain (C); MRI after scalp editing (D); original SPECT image coregistered to MRI (E); MR image segmented into white matter (F) and grey matter (G); White matter SPECT image (H) simulated from convolved white matter MR image; convolved grey matter MR image (I); white matter MR images (J); grey matter SPECT images (K) obtained by subtraction of simulated white matter SPECT image from original SPECT image coregistered to MRI; binary mask for grey matter (L) applied to finally obtain grey matter SPECT image corrected for partial volume effect (M). (Reprinted from ref.[45] with permission).

scheme one step further by incorporating a distinct volume-of-interest (VoI) such as the amygdale.[46] Their method consists first in solving the problem of white matter contribution by using Eq. (33). Subsequently, true cortical activity concentration is measured from the corrected image given in Eq. (34). The corrected image for the amygdala is then given by:

$$T_{VOI}(r) = \frac{g(r) - T_1 f_1(r) \otimes h(r) - T_2 f_2(r) \otimes h(r) - T_3 f_3 \otimes h(r)}{f_{VOI}(r) \otimes h(r)} \tag{35}$$

The "true" cortical value T_1 derived from the "white matter and CSF-corrected image" given in Eq. (34), must satisfy the following criteria:

(i) it must be representative of the true cortical grey activity that actually contaminates the VoI;
(ii) it must be sufficiently far from the VoI to avoid integrating some of its signal.

We can see that those two criteria might rapidly introduce some conflict with increasing tracer heterogeneity, and would be for example violated if one seeks to account for cross-contamination between e.g., the caudate nucleus and the Putamen since they are lying so close to each other.

6.3.2 Model-based Approach

Another type of post-reconstruction correction methods is the model-based optimization method developed by Chen *et al.*[42] to simultaneously recover the size and the activity concentration of small spheroids thus improving estimates of lesion activity in clinical oncology when object size is unknown (Figure 7). The algorithm is based on a 3D spatially varying object size- and contrast-dependent Gaussian model of the system PSF. A match index is then used to estimate the best model parameters. The authors report a reduction in the activity error by 11%-63% compared to the error obtained without correction. Moreover, the accuracy of the simple RC method is dependent on object-to-background ratio (OBR) and the data used for estimating fitting parameters. Large errors were reported for small spheroids, which are obviously very sensitive to OBR variation and noise. A modified version of the algorithm described above combined with an extension to non-spherical objects was recently proposed.[47] The method is being improved currently allowing the quantification of lung tumours with smallest radii with improved convergence properties towards the true model.

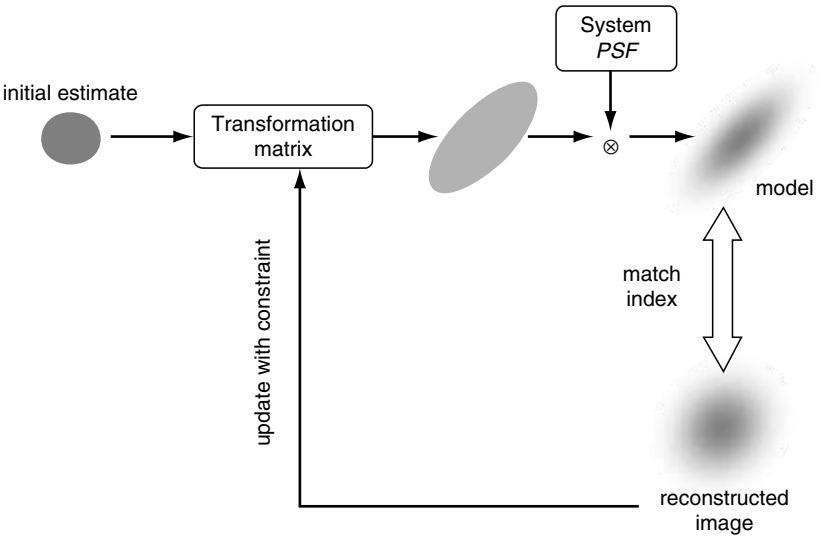

FIGURE 7. Description of the model-based method for partial volume correction in clinical oncology.[42]

6.3.3 Geometric Transfer Matrix (GTM) Approach

If we directly compute the effect of signal degradation due to limited spatial resolution on the mean regional concentration within a limited region of space, or region-of-interest (RoI[1]), we can obtain as many equations as there are unknowns. This is the basis for the method proposed by Rousset *et al.*[23,24,48] which allows for the calculation of corrected estimates without *a priori* knowledge on any activity level. For instance, the observed activity t_j within tissue component D_j from a given RoI_j is given by:

$$t_j = \sum_{i=1}^{N} \omega_{ij} T_i \tag{36}$$

where T_i represents the true tracer concentration within tissue component i. The weighting factors ω_{ij} represent the fraction of true activity T_i from tissue i that is integrated in the measurement t_j from RoI_j of volume v_j. They can be expressed as:

$$\omega_{ij} = \frac{1}{v_j} \int_{ROI_j} RSF_i(r)dr \tag{37}$$

where $RSF_i(r)$ represents the regional spread function of tissue i and corresponds to the response of the scanner to the distribution of activity D_i:

$$RSF_i = \int_{D_i} h(r, r')dr' \tag{38}$$

The weighting factors ω_{ij} constitute the geometric transfer matrix (GTM) and express the distortions introduced by the limited intrinsic spatial resolution of the scanner, as well as smoothing introduced during image back-projection, and further modulation during extraction of regional tracer concentration (RoI analysis). Both the effect of type and size of filter used during FBP[49] as well as definition of RoI[50,51] have been shown to introduce bias in parameter estimates.

In practice, these partial volume factors are computed from simulation of the noise-free *RSF* images and sampling with a user-defined set of RoIs. The number of RoIs must be equal to the number of tissue components identified in the tracer model in order to provide a full-rank GTM. In that case, the diagonal terms of the GTM represent the tissue self-recovery *RC* (or "spill-out") while off-diagonal terms ($\omega_{ij}, j \pm i$) represent the spill-over, or "spill-in", factors. If the number of RoIs is greater than N, the problem is over-constrained and can be solved by ordinary linear least square regression. The same set of RoIs must be used to extract observed values from the

[1]sample of image pixels for average radioactivity concentration computation

actual PET images in order to obtain the vectors t_j (tissue time-activity curves). The set of linear equations can then be solved for the true tracer concentration in each region by inverting the GTM matrices and multiplying by the observed regional values.[23,24,48]

This method was initially developed based on the simulation of sinogram data, in order to reproduce very accurately the effect of finite sampling and backprojection. This further allows for the incorporation of Poisson noise at the detector level for more realistic computer simulations of radioligand uptake for validation purposes.[23,48] It has since been shown that instead of simulating the *RSF* images from sinogram data, one can achieve similar levels of accuracy by creating the *RSF* images by direct convolution of the individual D_i maps with a kernel representative of the spatial resolution of the PET image.[52] This method can be seen as the image-based variant of the GTM method, and is much faster to implement without apparent sacrifice in data accuracy. Nonetheless, the sinogram approach has the advantage of being independent of the filter used during image reconstruction since it uses the same filter and FBP algorithm as the original PET data.

7. Performance Evaluation of Partial Volume Correction

Like any other correction algorithm, PVC methods must be validated and their limit tested before being applied to clinical or research data. This includes the assessment of the accuracy of the algorithm and its sensitivity towards methodological considerations such as simulation of the system's *PSF*, MR-ET image registration and MR image segmentation.

Absolute measurement of accuracy is only attainable in phantom and simulation studies. Accuracy is usually given as a percentage of the true activity, or can be expressed by the apparent recovery coefficient (*ARC*), which represents the apparent (observed or partial volume corrected) regional radioactivity concentration to true activity ratio.[23,48,52] Precision, or data reproducibility, is a more subjective measure of performance and will depend to a great extent on the level of automation of data analysis and correction. Methods that do not require human intervention may have a great level of reproducibility, but particular attention needs to be paid to accuracy of unsupervised methods.

7.1 Registration and Segmentation Errors

Post-reconstruction partial volume correction methods requiring additional anatomical information from e.g., MR imaging, such as the pixel-based approach or the GTM approach, rely on the spatial realignment of functional and anatomical images. Usually, a rigid-body transformation is used, with spatial transformation parameters being derived from the minimization of the distance between homologous points found in both modalities, or increasingly based on some similarity criterion between the two images.

These include methods such as Woods' popular minimization of the variance of ratio between the 2 images to be registered.[53] Other similarity criteria, such as the maximum cross-correlation54 or mutual information,[55] are also popular methods for image realignment.[56] The final image resolution, signal-to-noise ratio, and contrast in the image, all condition the success of the registration (see chapter 9).

The accuracy of the partial volume correction method will depend in part on the degree of accuracy in the realignment of the anatomical images with the emission image of tracer distribution. This has been investigated for both the pixel-based method[22,46,57,58] as well as for the GTM approach.[24,52,58,59] For the GTM approach, it is interesting to note that errors introduced during mis-registration only affect the observed estimates, and does not modify the coefficients of the GTM matrix. As a consequence, the registration error effect on the corrected estimates is of the same magnitude as the effect of mis-registration on the observed estimates due to poor RoI placement.[59] Those errors have been found to have relatively little impact (<2% of true value for typical 1-2 mm mis-registration error) on the final accuracy of the corrected estimates.[52,59] As for errors in segmentation of the tissue components of the system, they have been found to be of greater significance with for example a 5% decrease in Caudate Nucleus *ARC* if a 25% error in total volume is made.[52] However, it has been shown that the effect of the segmentation error was limited to the mis-segmented region.[52] Overall, it appears that the success of the segmentation of the structural information provided by e.g., MR images, has a higher impact on the accuracy of the corrected estimates,[60] compared to the influence of image co-registration, although some authors recently suggested that mis-registration errors have the strongest impact on data accuracy and precision.[58] This recent finding is also in contradiction with the conclusion achieved in the case of the performance evaluation of the method proposed by Müller-Gärtner.[22,57] The accuracy of this latter method further depends upon the accuracy in measurement of background (i.e., white matter) activity concentration. This error has been evaluated as being in the order of 5% error in grey matter (GM) PET estimate for a 20% error in white matter tracer concentration.[22]

As for the overall performance, i.e., in the absence of major sources of registration or segmentation errors, partial volume corrected estimates have been found to be typically within 5-10% of true tracer concentration with a standard deviation of a few percent in both phantom and simulation studies.[24,48,52,58,59,61]

7.1.1 Tissue Homogeneity

Segmentation errors can be thought as a more general problem of tissue heterogeneity. Indeed, the major limiting factor of those methods is primarily the assumption made about the homogeneity of tracer distribution in

each identified, or segmented, tissue components. Aston and colleagues have proposed a test of inhomogeneity based on Krylov subspace iteration that can test for hypothesis on homogeneous tracer distribution.[61] This would however only be effective in the case where the specified noise model is sufficiently accurate, which still remains a difficult endeavour.

However, if known, the tissue mixture of each identified component can be used to compute the various regional spread functions (Eq. 35). This is achieved by the use of statistical probabilistic anatomical maps (SPAM's)[62] that represent the probability of each tissue class (e.g., GM, WM, CSF) to be present in a given location of a standardized, or stereotaxic space.

7.1.2 Data Precision

Even if the registration, segmentation, or other homogeneity errors were inexistent, like any type of "deconvolution" procedure, compensating for partial volume effects will result in some degradation of the precision of the processed data. The variance associated with the corrected estimates can be estimated by explicit study of the covariance nature of the correction method. The degradation of the coefficient of variation (std/mean) after/before PVC can be seen as the noise magnification factor (*NMF*) resulting from the correction.[24] Maximum theoretical values of the NMF can be easily predicted for the GTM method and have shown to be in good agreement with experimental values derived from a brain phantom experiment.[24] Variance associated with the correction has been shown to only slightly increase after partial volume correction[23,24,48,52] suggesting the applicability of GTM-PVC to dynamic emission studies.[63,64]

7.2 Simulation Studies

Computer simulations are a powerful way to explore the limits of correction algorithms since they give a complete control to the operator. By reproducing realistic noise characteristics associated with emission tomography, one can demonstrate the usefulness of PVC algorithms and their applicability for a wide range of realistic situations. Another powerful application of computer simulation is the replication of methodological flaws and their consequence on image quantitation. These include simulation of erroneous definition of the scanner's *PSF*, registration errors between MR/CT and PET/SPECT, segmentation errors, and assumptions made about homogeneity of tracer distribution.

Computer simulation of emission tomography images would usually consist in reproducing the 4-D spatial distribution of the tracer in a digitized model of the organ of interest, and mimicking the geometry and other physical effects specific to the scanner.

7.2.1 Simulation of Objects

Simulation can consist in using mathematical models of simple shaped objects such as spheres or ellipses. For example, Mullani[65] designed a special phantom to measure the quantitative recovery of myocardial emission tomography images as a function of the size of the object and the angulation of a 1-cm-thick simulated myocardium inclined with respect to the image plane. Muzic *et al.*[41] used a set of 5 different elliptical models as part of their validation for the proposed PVC method applied to myocardial PET. This mathematical model represented the porcine torso including the lungs, myocardium, ventricular cavity, and soft tissue background.

Early digital phantoms were derived from post-mortem brain slices and used to evaluate the signal-to-noise performance with decreasing detecting crystal size.[66-68] A digitized version of the Data Spectrum sphere phantom was used for the evaluation of the Müller-Gärtner method.[57]

More recently, the development of classification and segmentation techniques applied to MR or CT images have allowed for the creation of numerical anatomical models of the spatial distribution of the parameter of interest. Digitized models can be a carefully segmented single individual MR volume[69] or models derived from the average of repeated high-resolution images of the same subject.[70] Atlases derived from tissue probability maps have become a popular way for automatic image segmentation,[71] and can be applied to individual data sets to create customized numerical phantoms. Simulated MR images can also be used to investigate the impact of MR image quality on segmentation accuracy[60,72] and could be used to study its subsequent effect on the accuracy of partial volume corrected estimates.

Those objects can be subject to local or global deformations to simulate a variety of situations. For example, the effect of tissue atrophy can be simulated to estimate the effect of a reduced brain structure volume on expected observed estimates.[73] Segmentation error can be simulated by erosion or dilation of the structure of interest and assess the resulting effect on the corrected estimates.[52,58]

7.2.2 Simulation of Image Formation Process

The effect of finite spatial resolution is usually reproduced either at the projection level, or directly in image space. The latter allows for a much faster implementation but does not offer the possibility of adding appropriate noise characteristics that are hard to define in image space. Adding appropriate noise to the image data is necessary for assessing the accuracy and precision of the correction technique in the presence of noise conditions comparable to that encountered in clinical practice. On the other hand, simulation of sinogram data allows for incorporation of the scatter component and the effect of attenuation at the detector level. This provides an opportunity to reproduce the propagation of Poisson noise encountered in a

more realistic way. Further, filtered backprojection type of image reconstruction is still widely used despite the forthcoming of reliable iterative reconstruction schemes for emission tomography (see Chapter 4). Smoothing the projection before projecting them back onto the image grid will get rid of a lot of the high-frequency noise, and will modulate both the magnitude of the signal—further degrading spatial resolution—and the characteristics of the noise.

Monte Carlo simulations represent a powerful way to reproduce the physics occurring in emission tomography (see Chapter 11). Similar to popular analytical simulators, simulated PET or SPECT images derived from Monte Carlo simulations can be used for validation of partial volume correction methods. In particular, Monte Carlo-based generation of projection data typical of [^{18}F]-dopa and [^{11}C]-raclopride uptake have been simulated using a digitized brain phantom[69] to assess the recovery capability of the GTM algorithm.[52]

7.2.3 Simulation of Tracer Kinetics

Simulation of the dynamic uptake of PET tracers such as neuroreceptor ligands, allows for testing the PVC capability to recover known distributions, both in terms of raw activity concentrations, and in terms of physiological parameters extracted from the kinetic modelling process. Tissue time-activity curves (TAC's) can be derived from individual emission data, corrected for partial volume effects using the GTM approach, and then fitted with a mathematical model normally used for extracting meaningful physiological parameters. The fitting curves can then be taken as true TAC input, assigned to the various tissue components identified from anatomical source, and processed through the simulator. This provides a convenient way for studying for example the effect of cortical grey matter heterogeneity on subcortical PVC estimates for various levels of heterogeneity and for varying contrast conditions.[74] More generally, this allows testing the performance of the PVC algorithms in noisy conditions similar to those expected or seen in clinical and research setting.

7.3 Experimental Phantom Studies

As discussed at the beginning of the previous section, physical phantoms can be used to directly derive correction factors. Those phantoms are limited in terms of their applicability due to the limitation in complexity one can achieve in reproducing the organ under study. However, physical phantom experiments are mostly used for validation purposes and represent the *sine qua non* step for proper acceptance of the technique. Physical phantoms of various degree of complexity can be used to demonstrate that the PVC algorithm works well for known distributions of radioactivity. They include simple geometrical objects with one, two, or all three dimensions suffering

from PVE for which the analytical expressions of quantitative recovery are available (cf. Eqs. 19-24). Validation is usually sought out by first making sure the partial volume correction method works for simple geometrical shapes such as cylinders or spheres. For example, a set of 5 spheres of various sizes was used for the validation of the simulated *PSF* used in the GTM-PVC algorithm.[24] Validation is further carried out with phantoms of increased complexity, with possible multiple isotope experiments for simulating time-varying contrast.[52] Realistic phantoms containing several independent compartments surrounded by a realistic medium, such as the brain phantom used to validate the GTM approach[24,48] represents more realistic imaging conditions. Those models are suitable for neuroreceptor studies where the tracer accumulates specifically in the striatum. For tracers diffusing more homogeneously throughout the cortex, an anthropomorphic phantom (STEPBRAIN) separating the cortex from white matter has been proposed.[75]

7.4 Clinical and Research Studies

7.4.1 Brain Imaging

Because of limitations of spatial resolution, quantitative PET measurements of cerebral blood flow, glucose metabolism and neuroreceptor binding, are influenced by partial-volume averaging among neighbouring tissues with differing tracer concentrations.[1] Partial volume effects are important for describing the true functional contribution of nuclear medicine images.[76] Decomposition of these images into a functional and structural component is necessary for studies of healthy ageing and pathophysiology, as well as for assessing clinical patients.[3,63]

Several algorithms have been proposed to improve positron emission tomography quantification by combining anatomical and functional information. The anatomical information could also be used to build an attenuation map for attenuation and scatter correction purposes.[77] The precision of these methods when applied to real data depends on the precision of the manifold correction steps, such as *PSF* modelling, magnetic resonance imaging-positron emission tomography registration, tissue segmentation, or background activity estimation. A good understanding of the influence of these parameters thus is critical to the effective use of the algorithms.[20,24,78] It has been shown that a two-compartment approach is better suited for comparative PET/SPECT studies, whereas the three-compartment algorithm is capable of greater accuracy for absolute quantitative measures.[57]

Several neuroimaging studies have attempted to verify the neurophysiologic correlates of age-related changes in the brain. In the early 1980s, using the ^{133}Xe inhalation method, researchers investigated cerebral blood flow and reported significant reductions with age. Since these pioneering studies, which suffered from poor spatial resolution and other limitations, the advent

of PET has provided neuroscientists with more sophisticated tools for the quantitative measurements of brain physiology.[25] Cerebral volume loss resulting from healthy aging processes can cause underestimation of PET physiologic measurements, despite great improvement in scanner resolution.[79] Thus, the failure to account for the effect of partial-volume averaging of brains with expanded sulci has contributed to the confounding results in functional imaging studies of aging. After partial volume correction, no CBF decline with age in healthy individuals is described.[44,80]

It is therefore expected that an important contribution to PET and SPECT imaging of the brain will be obtained by enhanced reconstruction algorithms incorporating resolution recovery techniques. An example of such method applicable to clinical data is a data-driven automated deconvolution approach.[81] Promising results to achieve such goal have been obtained by several authors e.g. using probabilistic MRI segmentation, subsequent binarization and convolution to obtain dispersion coefficients.[52]

Although different statistical mapping methods may yield grossly similar patterns of hypometabolism or hypoperfusion, the extent, severity, and peak location of metabolic changes can be inconsistent. Deformation accuracy appears to be more prone to atrophy.[82] Accurate estimates of striatal uptake and BP in ^{123}I brain SPECT are feasible with PVC, even with small errors in registering SPECT with anatomic data or in segmenting the striata.[64] In various pathological conditions, PVC can assess the functional contribution to pathology. Reduced glucose metabolism measured by PET in DAT is not simply an artefact due to an increase in CSF space induced by atrophy, but reflects a true metabolic reduction per gram of tissue.[83] Also in epileptic foci, hypometabolism is larger than a mere atrophy effect.[84]

It has been demonstrated that cerebral atrophy could not solely account for the loss of tissue function seen in DAT.[85] Conversely, when the same type of dilution correction is applied in the case of the study of normal aging, partial volume correction annihilates the significant decrease in cerebral blood flow in normal aging commonly reported before atrophy correction.[44] This is in disagreement with several earlier reports of decreased metabolism with normal aging.[86,87]

Brain perfusion studies performed in patients with probable DAT showed that rCBF was decreased in the parahippocampal gyrus but not in the hippocampus after pixel-based partial volume correction.[88] It was also demonstrated that the apparent decrease in uptake of a muscarinic cholinergic antagonist seen in temporal lobe epilepsy was due to a decrease in hippocampal volume rather than a decrease in receptor concentration.[89] This correction was based on global scaling by total measured volume of hippocampus from MRI.

Dopamine transporters have been shown to be markedly reduced in Lesh-Nyhan disease, partial volume correction only accentuating this finding.[73] Dopa-decarboxylaze activity has been shown to be greatly reduced in patients with Parkinson disease compared to normal controls.[63]

Studies of the dopaminergic system with SPECT have been shown to greatly benefit from partial volume correction using a striatal phantom modelling the basal ganglia[90] and a numerical model of the RSD brain phantom.[64] The latter study has shown that the bias in binding potential can be reduced from 50% to about 10%.

7.4.2 Myocardial Imaging

Several investigators have proposed to compute recovery coefficients and spillover factors from geometric measurement directly from the image[91] or derived from phantom studies.[92] In both cases, count recovery and spillover factors are derived by convolving the *PSF* in one dimension with an analytical model of the heart, comprised of a centre circle (blood pool or radius R) surrounded by an annulus (myocardium or thickness d), both of uniform activity. In this case, the *PSF* being considered as spatially invariant, the recovery coefficient for the blood pool corresponds to that of a 2-D cylindrical object or diameter $2R$, and can be expressed as (see Eq. 22):

$$F_{BB} = 1 - e^{-R_2/2s^2} \tag{39}$$

Similarly, the contribution of the blood pool to the myocardium F_{BM}, the self recovery of muscle tissue F_{MM}, and the contribution of the myocardial tissue to the blood compartment F_{MB} can be computed using the convolution integrals over the myocardium/ventricle model. They can be derived using formulas recalled in section 5. The original work of Henze and colleagues[91] proposed to extract the myocardium thickness and left ventricle diameter directly from PET using specific markers of the 2 regions. Herrero *et al.*, derived computed recovery and spillover factors using the same analytical procedure, but computed the dimensions of the left ventricle and myocardium wall from the dimensions of a standard heart phantom[92] (Data Spectrum, Hillsborough, NC).

Based on the assumption that partial volume errors are the same for transmission and emission images, it was demonstrated that the activity per gram of extravascular tissue can be estimated by dividing the perfusion regional data by extravascular density for the same region.[36] It is worth emphasizing that no convincing evidence was found of thickness above the partial volume limit in a large sample of 75 normotensive and 25 hypertensive patients.[93] Therefore it is likely that relations between myocardial count increases and wall thickening are similar throughout the cardiac cycle, even in patients with left ventricular hypertrophy. Using PET and $^{13}NH_3$-ammonia for the quantification of myocardial blood flow, Nuyts *et al.*[94] have obtained recovery coefficients of 59% for the myocardial wall and 86% for the blood pool in animal experiments. In addition, spillover from the blood pool into the myocardial was ~14%.

More recently, some authors have proposed to use correlated anatomical images to derive correction maps for partial volume in myocardial perfusion

studies. For instance, the group from UCSF has used CT images to define regional myocardial attenuation and count recovery maps of the porcine heart.[27] This method is similar to the pixel-by-pixel approach used for simple atrophy correction in brain PET,[43,95] although it does not provide corrected maps of the myocardium perfusion, but rather an average regional value.

7.4.3 Oncology Imaging

Despite the widespread applications of nuclear imaging (especially PET) in oncology, only a limited number of studies investigated the PVE problem in tumour imaging. The effects of object shape, size and background on SPECT ^{131}I activity quantification without detector response compensation has been reported in a detailed Monte Carlo study.[96] The activity quantification was carried out using a constant calibration factor and no PVC. It has been shown that the bias increases significantly with decreasing lesion size as a result of the increased spill-out of counts. More importantly, the bias for cylindrical lesions is consistently higher than for spherical lesions because spill-out is more significant for non-spherical objects. The bias also depends significantly on tumour-to-background ratio (TBR) because of the spill-in effect.

The simplest approach relies on the use of pre-calculated recovery coefficients for more reliable estimate of the standardized uptake value in pulmonary lesions.[97,98] The bias affecting TBR estimates owing to PVE is lesion size dependent. The generally accepted criterion is that PVC is required if the lesion size is less than 2-3 times the spatial resolution (FWHM) of the imaging system when the parameter of interest is the maximum voxel value within a particular VoI. In fact, Soret *et al.*[99] have demonstrated that when the parameter of interest is the average count density, the bias introduced by the PVE could exceed 10% even for lesions $\sim$6 times the FWHM depending on the true TBR.

Notwithstanding the known limitations, small animal imaging with a clinical dual-modality PET/CT scanner has been shown to be feasible for oncological imaging where the high resolution CT could be used for more precise localization of PET findings in addition to PVC through size-dependent recovery coefficient correction.[100] An aspect which deserves further attention is that robust models have also been developed to correction for partial volume effect in helical CT.[101]

8. Summary

Partial volume correction of emission tomography data remains a priority for accurate image quantitation. The ability to compensate for partial volume effects usually requires to: (1) characterize the point-spread function of the imaging system, (2) characterize the tissue components that participate in

the uptake and metabolism of the tracer, and (3) characterize the resolution effects in terms of correction factors or maps.

The imaging system *PSF* can be accurately measured by phantom experiments and is easily modelled by simple mathematical functions such as Gaussian or a series of Gaussian functions depending on whether the scatter component is included at that level or not. With the growing availability of multimodality integration and processing software, additional anatomical information provided by MR or CT imaging can be used to segment the distribution of the tracer into functionally meaningful regions. By studying the interaction of the system's *PSF* with a model of the tracer distribution, the contribution of each distinct region to the emission image can be computed. These interactions can be modelled using sophisticated Monte Carlo simulation, analytical projectors, or a simple convolution with a defined resolution kernel in image space.[102]

In practice self-recovery (*RC*) and spillover (or "spill-in") factors can be easily extracted and processed through any given set of user-defined *a priori* or *a posteriori* RoIs,[23,24,48] or *RC* maps and spill-in contributions can be derived to create images of the corrected radioactivity distribution in cortical grey matter.[22,25] With increased image resolution, the limit in size of regions that PVC can be applied to will constantly be pushed further, and it will become increasingly important to be able to account for cross-contamination of activity between small adjacent regions for which the assumptions made during the application of the pixel-based method[22] will be largely violated. The GTM approach[24] possesses the formidable advantage of not requiring any assumption of any tracer level at any time. The extraction of the GTM matrix is a one-time process, and does not require any additional computation for dynamic data, i.e., the same inverse of the GTM matrix is applied to all the data points since it expresses geometric interaction between the imaging system and the tissue component, independent of the contrast present in the image. Comparative assessment of PVC strategies is an important part of the validation step.[52,58,103]

Those methods proved to be sufficiently accurate to be applied in a growing number of research studies, if one considers that the number of publications related to the effect of the application of PVC algorithms to research data has grown significantly in the past few years. PVC is now a powerful and reliable tool that should become systematically used in research or clinical studies involving the use of emission tomography. It is expected that improvement in all aspects of the prerequisite for accurate partial volume correction are still required, especially for what concerns the quality of anatomo-functional mapping needed for accurate quantitation of cell-specific function and metabolism.

Acknowledgments. OR was supported by the National Institute of Neurological Disorders and Stroke (NINDS) under grant number

R01NS38927 and by the National Institute on Alcohol Abuse and Alcoholism (NIAAA) under grant number R01AA12839. HZ was supported by the Swiss National Science Foundation under grant SNSF 3152A0-102143.

References

1. Zaidi H. and Sossi, V., Correction for image degrading factors is essential for accurate quantification of brain function using PET. *Med Phys* **31:** 423-426 (2004).
2. Links J. M., Lesion detectability and quantitative recovery with FDG-PET. *Eur J Nucl Med* **26:** 681-682 (1999).
3. Fazio F. and Perani, D., Importance of partial-volume correction in brain PET studies. *J Nucl Med* **41:** 1849-1850 (2000).
4. Brooks R. A. and Di Chiro, G., Slice geometry in computer assisted tomography. *J Comput Assist Tomogr* **1:** 191-199 (1977).
5. Gautschi W., "Error functions and Fresnel integrals." in: *Handbook of Mathematical Functions*, edited by Abramowitz M and Segun I A Dover, New-York, (1968), *pp* 295-330.
6. Abramowitz M. and Segun, I. A., *Handbook of Mathematical Functions*, Dover publications, New-York, (1965).
7. Kessler R. M., Ellis, J. R. and Eden, M., Analysis of emission tomographic scan data: limitations imposed by resolution and background. *J Comput Assist Tomogr* **8:** 514-522 (1984).
8. Hoffman E. J., Huang, S. C., Plummer, D. *et al*., Quantitation in positron emission computed tomography: 6. effect of nonuniform resolution. *J Comput Assist Tomogr* **6:** 987-999 (1982).
9. Hoffman E. J., Huang, S. C. and Phelps, M. E., Quantitation in positron emission computed tomography: 1. Effect of object size. *J Comput Assist Tomogr* **3:** 299-308 (1979).
10. Mazziotta J. C., Phelps, M. E., Plummer, D. *et al*., Quantitation in positron emission computed tomography: 5. Physical–anatomical effects. *J Comput Assist Tomogr* **5:** 734-743 (1981).
11. Herscovitch P., Auchus, A. P., Gado, M. *et al*., Correction of positron emission tomography data for cerebral atrophy. *J Cereb Blood Flow Metab* **6:** 120-124 (1986).
12. Wahl L. M., Asselin, M. C. and Nahmias, C., Regions of interest in the venous sinuses as input functions for quantitative PET. *J Nucl Med* **40:** 1666-1675 (1999).
13. Huesman R. H., A new fast algorithm for the evaluation of regions of interest and statistical uncertainty in computed tomography. *Phys Med Biol* **29:** 543-552 (1984).
14. Tsui B. M., Hu, H., Gilland, D. *et al*., Implementation of simulataneous attenuation and detector response in SPECT. *IEEE Trans Nucl Sci* **35:** 778-783 (1988).
15. Zeng G. L., Gullberg, G. T., Bai, C. *et al*., Iterative reconstruction of fluorine-18 SPECT using geometric point response correction. *J Nucl Med* **39:** 124-130 (1998).

16. King M. A. and Miller, T. R., Use of a nonstationary temporal Wiener filter in nuclear medicine. *Eur J Nucl Med* **10:** 458-461 (1985).
17. Links J. M., Jeremy, R. W., Dyer, S. M. *et al*., Wiener filtering improves quantification of regional myocardial perfusion with thallium-201 SPECT. *J Nucl Med* **31:** 1230-1236 (1990).
18. Links J. M., Becker, L. C., Rigo, P. *et al*., Combined corrections for attenuation, depth-dependent blur, and motion in cardiac SPECT: a multicenter trial. *J Nucl Cardiol* **7:** 414-425 (2000).
19. Iida H., Kanno, I., Takahashi, A. *et al*., Measurement of absolute myocardial blood flow with H215O and dynamic positron-emission tomography. Strategy for quantification in relation to the partial-volume effect. *Circulation* **78:** 104-115 (1988).
20. Iida H., Law, I., Pakkenberg, B. *et al*., Quantitation of regional cerebral blood flow corrected for partial volume effect using O-15 water and PET: I. Theory, error analysis, and stereologic comparison. *J Cereb Blood Flow Metab* **20:** 1237-1251 (2000).
21. Chawluk J., Alavi, A., R, D. *et al*., Positron emission tomography in aging and dementia: effect of cerebral atrophy. *J Nucl Med* **28:** 431-437 (1987).
22. Muller-Gartner H. W., Links, J. M., Prince, J. L. *et al*., Measurement of radiotracer concentration in brain gray matter using positron emission tomography: MRI-based correction for partial volume effects. *J Cereb Blood Flow Metab* **12:** 571-583 (1992).
23. Rousset O., Ma, Y., Kamber, M. *et al*., 3D simulations of radiotracer uptake in deep nuclei of human brain. *Comput Med Imaging Graph* **17:** 373-379 (1993).
24. Rousset O. G., Ma, Y. and Evans, A. C., Correction for partial volume effects in PET: principle and validation. *J Nucl Med* **39:** 904-911 (1998).
25. Meltzer C. C., Kinahan, P. E., Greer, P. J. *et al*., Comparative evaluation of MR-based partial-volume correction schemes for PET. *J Nucl Med* **40:** 2053-2065 (1999).
26. Labbe C., Froment, J. C., Kennedy, A. *et al*., Positron emission tomography metabolic data corrected for cortical atrophy using magnetic resonance imaging. *Alzheimer Dis Assoc Disord* **10:** 141-170 (1996).
27. Da Silva A. J., Tang, H. R., Wong, K. H. *et al*., Absolute quantification of regional myocardial uptake of 99mTc-sestamibi with SPECT: experimental validation in a porcine model. *J Nucl Med* **42:** 772-779 (2001).
28. Chen C. H., Muzic, R. F., Nelson, A. D. *et al*., A nonlinear spatially variant object-dependent system model for prediction of partial volume effects and scatter in PET. *IEEE Trans Med Imaging* **17:** 214-227 (1998).
29. Brix G., Bellemann, M. E., Hauser, H. *et al*., [Recovery coefficients for the quantification of the arterial input functions from dynamic PET measurements: experimental and theoretical determination]. *Nuklearmedizin* **41:** 184-190 (2002).
30. Geworski L., Knoop, B. O., de Cabrejas, M. L. *et al*., Recovery correction for quantitation in emission tomography: a feasibility study. *Eur J Nucl Med* **27:** 161-169 (2000).
31. Blankespoor S. C., Xu, X., Kaiki, K. *et al*., Attenuation correction of SPECT using X-ray CT on an emission-transmission CT system: myocardial perfusion assessment. *IEEE Trans Nucl Sci* **43:** 2263-2274 (1996).
32. Sossi V., Buckley, K. R., Snow, B. J. *et al*., Recovery of the human striatal signal in a slice oriented positron emission tomograph. *J Nucl Med* **34:** 481-487 (1993).

33. Shepp L. A. and Vardi, Y., Maximum likelihood reconstruction for emission tomography. *IEEE Trans Med Imag* **1:** 113-122 (1982).
34. Hutton B. F. and Lau, Y. H., Application of distance-dependent resolution compensation and post-reconstruction filtering for myocardial SPECT. *Phys Med Biol* **43:** 1679-1693 (1998).
35. Pretorius P. H., King, M. A., Pan, T. S. *et al*., Reducing the influence of the partial volume effect on SPECT activity quantitation with 3D modelling of spatial resolution in iterative reconstruction. *Phys Med Biol* **43:** 407-420 (1998).
36. Hutton B. F. and Osiecki, A., Correction of partial volume effects in myocardial SPECT. *J Nucl Cardiol* **5:** 402-413 (1998).
37. Brix G., Doll, J., Bellemann, M. E. *et al*., Use of scanner characteristics in iterative image reconstruction for high-resolution positron emission tomography studies of small animals. *Eur J Nucl Med* **24:** 779-786 (1997).
38. Calvini P., Vitali, P., Nobili, F. *et al*., Enhancement of SPECT reconstructions by means of coregistered MR data. *IEEE Trans Nucl Sci* **48:** 750-755 (2001).
39. Kim H. J., Zeeberg, B. R. and Reba, R. C., Compensation for three-dimensional detector response, attenuation and scatter in SPECT grey matter imaging using an iterative reconstruction algorithm which incorporates a high-resolution anatomical image. *J Nucl Med* **33:** 1225-1234 (1992).
40. Ouyang X., Wong, W., Johnson, V. *et al*., Incorporation of correlated structural images in PET image-reconstruction. *IEEE Trans Med Imaging* **13:** 627-640 (1994).
41. Muzic R. F., Chen, C. H. and Nelson, A. D., A method to correct for scatter, spillover, and partial volume effects in region of interest analysis in PET. *IEEE Trans Med Imaging* **17:** 202-213 (1998).
42. Chen C. H., Muzic, R. F., Nelson, A. D. *et al*., Simultaneous recovery of size and radioactivity concentration of small spheroids with PET data. *J Nucl Med* **40:** 118-130 (1999).
43. Videen T. O., Perlmutter, J. S., Mintun, M. A. *et al*., Regional correction of positron emission tomography data for the effects of cerebral atrophy. *J Cereb Blood Flow Metab* **8:** 662-670 (1988).
44. Meltzer C. C., Cantwell, M. N., Greer, P. J. *et al*., Does cerebral blood flow decline in healthy aging? A PET study with partial-volume correction. *J Nucl Med* **41:** 1842-1848 (2000).
45. Matsuda H., Ohnishi, T., Asada, T. *et al*., Correction for partial-volume effects on brain perfusion SPECT in healthy men. *J Nucl Med* **44:** 1243-1252 (2003).
46. Meltzer C. C., Zubieta, J. K., Links, J. M. *et al*., MR-based correction of brain PET measurements for heterogeneous gray matter radioactivity distribution. *J Cereb Blood Flow Metab* **16:** 650-658 (1996).
47. Schoenahl F. and Zaidi, H., ''Towards optimal model-based partial volume effect correction in oncological PET.'' *Proc*. IEEE Nuclear Science Symposium and Medical Imaging Conference, Oct. 19-22, Rome, Italy, (2004) *in press*
48. Rousset O. G., Ma, Y., Marenco, S. *et al*., ''In vivo correction for partial volume effects in PET: accuracy and precision.'' in: *Quantification of brain function using PET*, edited by R. Myers, Cunningham, V., Bailey, DL, Jones, T Academic Press, San Diego, (1996), *pp* 158-165.
49. Spinks T., Guzzardi, R. and Bellina, C. R., Measurement of resolution and recovery in recent generation positron tomographs. *Eur J Nucl Med* **15:** 750-755 (1989).

50. Kuwert T., Ganslandt, T., Jansen, P. *et al.*, Influence of size of regions of interest on PET evaluation of caudate glucose consumption. *J Comput Assist Tomogr* **16:** 789-794 (1992).
51. Kuwert T., Morgenroth, C., Woesler, B. *et al.*, Influence of size of regions of interest on the measurement of uptake of 123I-alpha-methyl tyrosine by brain tumours. *Nucl Med Commun* **17:** 609-615 (1996).
52. Frouin V., Comtat, C., Reilhac, A. *et al.*, Correction of partial volume effect for PET striatal imaging: fast implementation and study of robustness. *J Nucl Med* **43:** 1715-1726 (2002).
53. Woods R. P., Mazziotta, J. C. and Cherry, S. R., MRI-PET registration with automated algorithm. *J Comput Assist Tomogr* **17:** 536-546 (1993).
54. Collins D. L., Neelin, P., Peters, T. M. *et al.*, Automatic 3D intersubject registration of MR volumetric data in standardized Talairach space. *J Comput Assist Tomogr* **18:** 192-205 (1994).
55. Maes F., Vandermeulen, D. and Suetens, P., Medical image registration using mutual information. *Proceedings of the IEEE* **91:** 1699-1722 (2003).
56. Robbins S., Evans, A., Collins, D. *et al.*, Tuning and comparing spatial normalization methods. *Lecture Notes in Computer Science* **2879:** 910- 917 (2003).
57. Strul D. and Bendriem, B., Robustness of anatomically guided pixel-by-pixel algorithms for partial volume effect correction in positron emission tomography. *J Cereb Blood Flow Metab* **19:** 547-559 (1999).
58. Quarantelli M., Berkouk, K., Prinster, A. *et al.*, Integrated software for the analysis of brain PET/SPECT studies with partial-volume-effect correction. *J Nucl Med* **45:** 192-201 (2004).
59. Slifstein M., Mawlawi, O. and Laruelle, M., "Partial volume effect correction: Methodological consideration." in: *Physiological Imaging of the Brain with PET.*, edited by SB Hansen A. Gjedde, GM Knudsen, OB Paulson Academic Press, San Diego, (2001), *pp* 67-75.
60. Zaidi H., Ruest T., Schoenahl F., Montandon M- L., Comparative assessment of brain MR image segmentation algorithms and their impact on partial volume correction in PET. (2004) *submitted*
61. Aston J. A., Cunningham, V. J., Asselin, M. C. *et al.*, Positron emission tomography partial volume correction: estimation and algorithms. *J Cereb Blood Flow Metab* **22:** 1019-1034 (2002).
62. Evans A., Marrett, S., Neelin, P. *et al.*, Anatomical mapping of functional activation in stereotactic coordinate space. *Neuroimage* **1:** 43-53 (1992).
63. Rousset O. G., Deep, P., Kuwabara, H. *et al.*, Effect of partial volume correction on estimates of the influx and cerebral metabolism of 6-[(18)F]fluoro-L-dopa studied with PET in normal control and Parkinson's disease subjects. *Synapse* **37:** 81-89 (2000).
64. Soret M., Koulibaly, P. M., Darcourt, J. *et al.*, Quantitative accuracy of dopaminergic neurotransmission imaging with 123I SPECT. *J Nucl Med* **44:** 1184-1193 (2003).
65. Mullani N. A., A phantom for quantitation of partial volume effects in ECT. *IEEE Trans Nucl Sci* **36:** 983-987 (1989).
66. Phelps M. E., Huang, S. C., Hoffman, E. J. *et al.*, An analysis of signal amplification using small detectors in positron emission tomography. *J Comput Assist Tomogr* **6:** 551-565 (1982).

67. Hoffman E., "Positron Emission Tomography: principles and quantitation." in: *Positron Emission Tomography and Autoradiography*, edited by Mazziotta JC and Schelbert HR Phelps ME Raven Press, (1986), *pp* 237-286.
68. Hoffman E. J., Cutler, P. D., Digby, W. M. *et al.*, 3-D phantom to simulate cerebral blood flow and metabolic images for PET. *IEEE Trans Nucl Sci* **37:** 616-620 (1990).
69. Zubal I. G., Harrell, C. R., Smith, E. O. *et al.*, Computerized 3-dimensional segmented human anatomy. *Med Phys* **21:** 299-302 (1994).
70. Holmes C. J., Hoge, R., Collins, L. *et al.*, Enhancement of MR images using registration for signal averaging. *J Comput Assist Tomogr* **22:** 324-333 (1998).
71. Collins D., Holmes, C., Peters, T. *et al.*, Automatic 3-D model-based neuroanatomical segmentation. *Human Brain Mapping* **3:** 190-208 (1995).
72. Shan Z. Y., Yue, G. H. and Liu, J. Z., Automated histogram-based brain segmentation in T1-weighted three-dimensional magnetic resonance head images. *Neuroimage* **17:** 1587-1598 (2002).
73. Wong D. F., Harris, J. C., Naidu, S. *et al.*, Dopamine transporters are markedly reduced in Lesch-Nyhan disease in vivo. *Proc Natl Acad Sci U S A* **93:** 5539-5543 (1996).
74. Rousset O. G., Ma, Y., Wong, D. F. *et al.*, "Pixel-versus region-based partial volume correction in PET." in: *Quantitative Functional Imaging with Positron Emission Tomography*., edited by RE Carson, Daube-Witherspoon, ME, Herscovitch, P Academic Press, San Diego, (1998), *pp* 67-75.
75. Alfano B., Brunetti, A., Prinster, A. *et al.*, "STEPBRAIN: a stereolithographed phantom of the brain for nuclear medicine: computed tomography, and magnetic resonance applications. (abstract)" Annual meeting of the Radiological Society of North America, Chicago, USA, (2003).
76. Szabo Z., Links, J. M., Seki, C. *et al.*, Scatter, spatial resolution, and quantitative recovery in high resolution SPECT. *J Comput Assist Tomogr* **16:** 461-467 (1992).
77. Zaidi H., Montandon, M.-L. and Slosman, D. O., Magnetic resonance imaging-guided attenuation and scatter corrections in three-dimensional brain positron emission tomography. *Med Phys* **30:** 937-948 (2003).
78. Law I., Iida, H., Holm, S. *et al.*, Quantitation of regional cerebral blood flow corrected for partial volume effect using O-15 water and PET: II. Normal values and gray matter blood flow response to visual activation. *J Cereb Blood Flow Metab* **20:** 1252-1263 (2000).
79. Braem A., Chamizo Llatas, M., Chesi, E. *et al.*, Feasibility of a novel design of high-resolution parallax-free Compton enhanced PET scanner dedicated to brain research. *Phys Med Biol* **49:** 2547-2562 (2004).
80. Van Laere K. J. and Dierckx, R. A., Brain perfusion SPECT: age- and sex-related effects correlated with voxel-based morphometric findings in healthy adults. *Radiology* **221:** 810-817 (2001).
81. Mignotte M., Meunier, J., Soucy, J.-P. *et al.*, Comparison of deconvolution techniques using a distribution mixture parameter estimation : application in SPECT imagery. *J Electron Imag* **11:** 11-25 (2002).
82. Ishii K., Willoch, F., Minoshima, S. *et al.*, Statistical brain mapping of 18F-FDG PET in Alzheimer's disease: validation of anatomic standardization for atrophied brains. *J Nucl Med* **42:** 548-557 (2001).

83. Ibanez V., Pietrini, P., Alexander, G. E. *et al*., Regional glucose metabolic abnormalities are not the result of atrophy in Alzheimer's disease. *Neurology* **50:** 1585-1593 (1998).
84. Knowlton R. C., Laxer, K. D., Klein, G. *et al*., In vivo hippocampal glucose metabolism in mesial temporal lobe epilepsy. *Neurology* **57:** 1184-1190 (2001).
85. Meltzer C. C., Zubieta, J. K., Brandt, J. *et al*., Regional hypometabolism in Alzheimer's disease as measured by positron emission tomography after correction for effects of partial volume averaging. *Neurology* **47:** 454-461 (1996).
86. Melamed E., Lavy, S., Bentin, S. *et al*., Reduction in regional cerebral blood flow during normal aging in man. *Stroke* **11:** 31-35 (1980).
87. Martin A. J., Friston, K. J., Colebatch, J. G. *et al*., Decreases in regional cerebral blood flow with normal aging. *J Cereb Blood Flow Metab* **11:** 684-689 (1991).
88. Matsuda H., Kanetaka, H., Ohnishi, T. *et al*., Brain SPET abnormalities in Alzheimer's disease before and after atrophy correction. *Eur J Nucl Med Mol Imaging* **29:** 1502-1505 (2002).
89. Weckesser M., Hufnagel, A., Ziemons, K. *et al*., Effect of partial volume correction on muscarinic cholinergic receptor imaging with single-photon emission tomography in patients with temporal lobe epilepsy. *Eur J Nucl Med* **24:** 1156-1161 (1997).
90. Koole M., Laere, K. V., de Walle, R. V. *et al*., MRI guided segmentation and quantification of SPECT images of the basal ganglia: a phantom study. *Comput Med Imaging Graph* **25:** 165-172 (2001).
91. Henze E., Huang, S. C., Ratib, O. *et al*., Measurements of regional tissue and blood-pool radiotracer concentrations from serial tomographic images of the heart. *J Nucl Med* **24:** 987-996 (1983).
92. Herrero P., Markham, J. and Bergmann, S. R., Quantitation of myocardial blood flow with H2 15O and positron emission tomography: assessment and error analysis of a mathematical approach. *J Comput Assist Tomogr* **13:** 862-873 (1989).
93. Nichols K., DePuey, E. G., Friedman, M. I. *et al*., Do patient data ever exceed the partial volume limit in gated SPECT studies? *J Nucl Cardiol* **5:** 484-490 (1998).
94. Nuyts H., Maes, A., Vrolix, M. *et al*., Three-dimensional correction for spillover and recovery of myocardial PET images. *J Nucl Med* **37:** 767-774 (1996).
95. Meltzer C. C., Leal, J. P., Mayberg, H. S. *et al*., Correction of PET data for partial volume effects in human cerebral cortex by MR imaging. *J Comput Assist Tomogr* **14:** 561-570 (1990).
96. Dewaraja Y. K., Ljungberg, M. and Koral, K. F., Monte Carlo evaluation of object shape effects in iodine-131 SPET tumor activity quantification. *Eur J Nucl Med* **28:** 900-906 (2001).
97. Vesselle H., Schmidt, R. A., Pugsley, J. M. *et al*., Lung cancer proliferation correlates with [F-18]Fluorodeoxyglucose uptake by positron emission tomography. *Clin Cancer Res* **6:** 3837-3844 (2000).
98. Menda Y., Bushnell, D. L., Madsen, M. T. *et al*., Evaluation of various corrections to the standardized uptake value for diagnosis of pulmonary malignancy. *Nucl Med Commun* **22:** 1077-1081 (2001).
99. Soret M., Riddell, C., Hapdey, S. *et al*., Biases affecting the measurements of tumor-to-background activity ratio in PET. *IEEE Trans Nucl Sci* **49:** 2112-2118 (2002).

100. Tatsumi M., Nakamoto, Y., Traughber, B. *et al*., Initial experience in small animal tumor imaging with a clinical positron emission tomography/computed tomography scanner using 2-[F-18]Fluoro-2-deoxy-D-glucose. *Cancer Res* **63:** 6252-6257 (2003).
101. Hsieh J., Nonlinear partial volume artifact correction in helical CT. *IEEE Trans Nucl Sci* **46:** 743-747 (1999).
102. Zaidi H., Relevance of accurate Monte Carlo modeling in nuclear medical imaging. *Med Phys* **26:** 574-608 (1999).
103. Koole M., Van de Walle, R., Van Laere, K. *et al*., Study of the quantification of FBP SPECT images with a correction for partial volume effects. *IEEE Trans Nucl Sci* **49:** 69-73 (2002).